Decadal variability in core surface flows deduced from geomagnetic observatory monthly means

Geophysical Journal International

Geophys. J. Int. (2016) **207,** 228–243
Advance Access publication 2016 July 20
GJI Geomagnetism, rock magnetism and palaeomagnetism

doi: 10.1093/gji/ggw268

Decadal variability in core surface flows deduced from geomagnetic observatory monthly means

K.A. Whaler,[1] N. Olsen[2] and C.C. Finlay[2]

[1]*School of GeoSciences, University of Edinburgh, Grant Institute, James Hutton Road, Edinburgh EH*9 3*FE, United Kingdom.*
E-mail: kathy.whaler@ed.ac.uk
[2]*DTU Space, Technical University of Denmark, Diplomvej* 371*, DK*-2800 *Kgs. Lyngby, Denmark*

Accepted 2016 July 18. Received 2016 July 17; in original form 2015 December 21

SUMMARY

Monthly means of the magnetic field measurements at ground observatories are a key data source for studying temporal changes of the core magnetic field. However, when they are calculated in the usual way, contributions of external (magnetospheric and ionospheric) origin may remain, which make them less favourable for studying the field generated by dynamo action in the core. We remove external field predictions, including a new way of characterizing the magnetospheric ring current, from the data and then calculate revised monthly means using robust methods. The geomagnetic secular variation (SV) is calculated as the first annual differences of these monthly means, which also removes the static crustal field. SV time-series based on revised monthly means are much less scattered than those calculated from ordinary monthly means, and their variances and correlations between components are smaller. On the annual to decadal timescale, the SV is generated primarily by advection in the fluid outer core. We demonstrate the utility of the revised monthly means by calculating models of the core surface advective flow between 1997 and 2013 directly from the SV data. One set of models assumes flow that is constant over three months; such models exhibit large and rapid temporal variations. For models of this type, less complex flows achieve the same fit to the SV derived from revised monthly means than those from ordinary monthly means. However, those obtained from ordinary monthly means are able to follow excursions in SV that are likely to be external field contamination rather than core signals. Having established that we can find models that fit the data adequately, we then assess how much temporal variability is required. Previous studies have suggested that the flow is consistent with torsional oscillations (TO), solid body-like oscillations of fluid on concentric cylinders with axes aligned along the Earth's rotation axis. TO have been proposed to explain decadal timescale changes in the length-of-day. We invert for flow models where the only temporal changes are consistent with TO, but such models have an unacceptably large data misfit. However, if we relax the TO constraint to allow a little more temporal variability, we can fit the data as well as with flows assumed constant over three months, demonstrating that rapid SV changes can be reproduced by rather small flow changes. Although the flow itself changes slowly, its time derivative can be locally (temporally and spatially) large, in particular when and where core surface secular acceleration peaks. Spherical harmonic expansion coefficients of the flows are not well resolved, and many of them are strongly correlated. Averaging functions, a measure of our ability to determine the flow at a given location from the data distribution available, are poor approximations to the ideal, even when centred on points of the core surface below areas of high observatory density. Both resolution and averaging functions are noticeably worse for the toroidal flow component, which dominates the flow, than the poloidal flow component, except around the magnetic equator where averaging functions for both components are poor.

Key words: Magnetic field; Rapid time variations; Core, outer core and inner core.

1 INTRODUCTION

The geomagnetic field is generated by and evolves in response to flow of electrically conducting liquid, predominantly iron, in the Earth's outer core. Therefore, temporal changes of the field can be used to obtain some information on that flow. For example, over the hemisphere centred on the Greenwich meridian, features of the field tend to drift west at a rate of a fraction of a degree per year, whereas the field over the other hemisphere changes more slowly. These observations can be reproduced by models of flow at the core–mantle boundary (CMB) with a band of westward motion straddling the equator moving at of order 10 km yr^{-1} in the western hemisphere, and much slower flow without obvious large-scale organization beneath the Pacific Ocean. However, inferring the flow from geomagnetic field changes is not straightforward, and involves making and testing a number of hypotheses as to its nature to reduce or eliminate the inherent non-uniqueness. CMB flow models, particularly those obtained after making additional dynamical assumptions about the force balance in the core (e.g. Le Mouël 1984), have proved to be a useful tool to probe the dynamics of the dynamo process responsible for maintaining the magnetic field.

The difficulties come in part from our incomplete knowledge of the geomagnetic field so far from where it is observed. The mantle is a weak electrical conductor, meaning that the field can be approximated as the gradient of a scalar potential throughout. This allows us to construct models of the field, and its temporal evolution or secular variation (SV), at the base of the mantle from observations at or near the Earth's surface. However, geometrical attenuation preferentially attenuates small-scale features, so they are known with less certainty there. This is accounted for in most modelling strategies by minimizing a measure of spatial roughness of the field (regularizing the solution) in addition to a measure of data misfit. The electrical conductivity jump from the assumed insulating mantle into the conducting liquid iron core means that only the radial component of the field and its SV is guaranteed to be continuous. Therefore, although we can use all observations of the field to construct the potential describing it at the CMB, we can only use its radial component to infer core flow.

The relationship between the field, its SV and the flow is given by the induction equation, a combination of Maxwell's equations in the appropriate limit:

$$\dot{\mathbf{B}} = \nabla \times (\mathbf{v} \times \mathbf{B}) + \eta \nabla^2 \mathbf{B}, \tag{1}$$

where $\mathbf{B}$ is the magnetic field, $\mathbf{v}$ the flow, and $\eta = \frac{1}{\mu_0 \sigma}$ is the magnetic diffusivity, where the core's electrical conductivity is σ, and its permeability is assumed to be that of free space, μ_0. The first term on the right-hand side represents advection of the field by the flow, that is, the flow carries field lines along with it; the second represents diffusion, that is, the creation and destruction of field lines. Below the CMB, we cannot estimate the field based on surface measurements as it has sources and sinks, meaning it can no longer be expressed as the gradient of a scalar potential; for the same reason, we cannot estimate vertical gradients of the field, even at the CMB, so the diffusive term of eq. (1) is unknown. Fortunately, it is possible to argue that SV arising from diffusion is negligible compared to that from advection, at least on the timescale of decades and shorter, and for large-scale magnetic fields, and so the second term on the right-hand side of eq. (1) can be ignored. This is known as the frozen-flux hypothesis, since, under this assumption, the field is perfectly frozen into the flow (Roberts & Scott 1965). Taking the radial component of eq. (1) at the CMB, neglecting the final term, gives

$$\dot{B}_r + \nabla_H . (\mathbf{v} B_r) = 0, \tag{2}$$

where ∇_H denotes the horizontal parts of the nabla operator. The term involving the (unknown) radial derivative of B_r does not appear in this equation because it multiplies v_r, which vanishes at the core surface since it is a material boundary. Hence, eq. (2) relates the known radial components of the magnetic field and its horizontal derivatives, and the radial component of the SV, to the unknown velocity. Unfortunately, it is a single equation in two unknowns: the horizontal components of the flow. This leaves an inherent ambiguity when we attempt to determine the flow, which was first recognized by Roberts & Scott (1965), and characterized by Backus (1968). Subsequently, a number of assumptions have been put forward that reduce or eliminate this ambiguity, many of which can be tested for consistency with the magnetic field and SV data (as can the frozen-flux hypothesis). Some of these put constraints on the magnetic field and flow within the core, so are particularly useful for interrogating the dynamical regime in which the geodynamo operates.

Here we solve a linear inverse problem for the flow based on eq. (2), assuming that it is large-scale (enforced through regularization). A further complication arises at this point: the smaller-scale components of the flow which we ignore can interact with small-scale features of the field (which we are unable to resolve from observations at the Earth's surface) to generate large-scale SV (Eymin & Hulot 2005). Voorhies & Backus (1985) show that assuming the flow is constant over a minimum of three epochs is sufficient to resolve its inherent non-uniqueness. The data are monthly estimates of SV at geomagnetic observatories, so our flows are assumed constant over a period of just three months - much shorter than the advective timescale appropriate for large-scale flows (Roberts & Scott 1965). We refer to these as snapshots of the flow.

Despite a wide range of inversion strategies—different data types, assumptions made to reduce the inherent non-uniqueness, regularization choices, whether the data misfit minimized is based on a two- or one-norm measure—many features of the flow appear to be robust. However, there has been little formal analysis of this aspect of the models, or their uncertainties and resolution. A recent study by Pais *et al.* (2015) used principal component analysis and singular value decomposition to determine the robust global features of the flow. We instead concentrate on the resolution of individual flow coefficients parametrizing our models, and calculate averaging functions that indicate our ability to reconstruct the flow at specified locations on the CMB; the averaging functions have a strong dependence on the distribution of the surface geomagnetic observatories providing the SV data. Working with SV data themselves, rather than parametrized models of them, permits this analysis.

Previous studies have found that a large part of the modelled SV can be explained by a steady flow on which is superimposed a set of oscillations of solid body-like flow on cylinders concentric with the rotation axis, known as torsional oscillations (TO; Zatman & Bloxham 1997). Cylinders of different radii oscillate at different rates, with periods thought to be typically of order a decade. TO are expected on dynamical grounds and allow angular momentum to be exchanged between the core and mantle. The CMB flow corresponding to TO is purely zonal, and symmetric with respect to the equator, and so can be described by a small number of flow coefficients. We test whether a flow whose only time variations are consistent with TO is an adequate fit to the SV data by seeking a model covering the whole time span of our study,

1997–2013, and minimizing changes in flow coefficients from epoch to epoch, except those corresponding to TO. We also calculate the minimum amount of change in the flow between epochs necessary to fit the data by restricting temporal variability in *all* flow coefficients.

In the next section we describe the model parametrization, and set up the inverse problem for the flow. The data we use in the inversion are described in Section 3, and the results, including flow coefficient resolution and averaging functions, in Section 4. We discuss the flows, particularly the implications of their temporal variability, in Section 5 and then present brief conclusions.

2 METHOD

Spherical harmonics are the natural basis functions for expressing the global magnetic field, which we assume is of internal origin. Away from sources, it is a potential field and can be written as the gradient of a scalar potential, V:

$$\mathbf{B} = -\nabla V(\theta, \phi, r), \tag{3}$$

where

$$V(\theta,\phi,r) = a\sum_{n=1}^{N}\sum_{m=0}^{n}\left(\frac{a}{r}\right)^{n+1} \times \left(g_n^m \cos m\phi + h_n^m \sin m\phi\right) P_n^m(\cos\theta) \tag{4}$$

and $P_n^m(\cos\theta)$ are Schmidt quasi-normalized associated Legendre functions of degree n and order m. θ, ϕ, r are spherical polar coordinates, that is, colatitude, longitude and radius, and a is a reference radius, here the Earth's mean radius. We assume that terms beyond the truncation level N can be neglected.

To explain changes of the field by advective flow, we decompose the velocity into its toroidal and poloidal parts:

$$\mathbf{v} = \nabla \times (\mathcal{T}\mathbf{r}) + \nabla \times \nabla \times (\mathcal{S}\mathbf{r}), \tag{5}$$

where $\mathcal{T}$ and $\mathcal{S}$ are the toroidal and poloidal scalars, respectively. As the CMB is a material surface across which there is no flow, eq. (5) simplifies there to

$$\mathbf{v}_H = \nabla \times (\mathcal{T}\mathbf{r}) + \nabla_H(r\mathcal{S}) \tag{6}$$

and both $\mathcal{T}$ and $\mathcal{S}$ average to zero over the CMB. Thus, they can also be expressed in spherical harmonics:

$$\mathcal{T} = \sum_{n=1}^{N_{\max}}\sum_{m=0}^{n}\left(t_n^{mc}\cos m\phi + t_n^{ms}\sin m\phi\right) P_n^m(\cos\theta)$$
$$\mathcal{S} = \sum_{n=1}^{N_{\max}}\sum_{m=0}^{n}\left(s_n^{mc}\cos m\phi + s_n^{ms}\sin m\phi\right) P_n^m(\cos\theta) \tag{7}$$

Again, we truncate the spherical harmonic expansions (at degree $N_{\max}$), by assuming the flow is large-scale.

Substituting spherical harmonic expansions for the CMB radial field and its SV (obtained from eqs 3 and 4 and their time derivatives with r set to be the core radius), and the flow, into eq. (2) and manipulating as described in, for example, Whaler (1986), we obtain a linear system of equations relating the SV coefficients to the flow coefficients, assuming the field coefficients are known:

$$\dot{\mathbf{g}} = \mathbf{E}\mathbf{t} + \mathbf{G}\mathbf{s} \tag{8}$$

where $\dot{\mathbf{g}}$ is a vector of SV coefficients $(\dot{g}_n^m, \dot{h}_n^m)$, and $\mathbf{t}$ and $\mathbf{s}$ are vectors of coefficients (t_n^{mc}, t_n^{ms}) and (s_n^{mc}, s_n^{ms}) respectively. $\mathbf{E}$ and $\mathbf{G}$ are matrices whose values depend on the main field coefficients and either Elsasser or Gaunt integrals, respectively (Whaler 1986).

Many previous studies have been based on inverting eq. (8) for the flow coefficients, treating SV coefficients as data. However, then it is very difficult to evaluate the error budget, as it is not clear how much of the misfit arises from a failure of the SV coefficients to fit the data from which they were derived. Hence following, for example, Whaler (1986), Waddington *et al.* (1995) and Beggan *et al.* (2009), we invert SV data directly for the flow. Our data are the North, East and vertically downwards orthogonal SV components $\dot{X}$, $\dot{Y}$ and $\dot{Z}$ respectively (related to the spherical polar components by $\dot{X} = -\dot{B}_\theta$, $\dot{Y} = \dot{B}_\phi$ and $\dot{Z} = -\dot{B}_r$) at the locations of geomagnetic observatories used in this study; we organize them into a vector $\dot{\mathbf{d}}$. They are linearly related to the coefficients $(\dot{g}_n^m, \dot{h}_n^m)$ through a matrix $\mathbf{Y}$ of appropriate spherical harmonic derivatives. Hence they are also linearly related to the flow, giving a system of equations

$$\dot{\mathbf{d}} = \mathbf{Y}\dot{\mathbf{g}} = \mathbf{Y}\mathbf{E}\mathbf{t} + \mathbf{Y}\mathbf{G}\mathbf{s} \equiv \mathbf{A}\mathbf{m} \tag{9}$$

where $\mathbf{m}$ is a vector of the unknown flow coefficients $\mathbf{t}$ and $\mathbf{s}$.

Eq. (9) forms the basis of our inverse problem. As already noted, a flow that is constant over three epochs (here, months) is formally unique (Voorhies & Backus 1985), but we also assume it is large-scale to overcome practical issues of ambiguity. Hence we regularize the inversion, ensuring that the flow spherical harmonic series (7) converge, with an appropriate value of the regularization parameter, λ_v, which controls the relative importance of fitting the data and forcing the flow to be large-scale. We thus calculate a series of $(n_{\text{epochs}} - 2)$ flow snapshot models, where n_{epochs} is the number of months for which we have data, using

$$\hat{\mathbf{m}} = (\mathbf{A}^T\mathbf{C}_e{}^{-1}\mathbf{A} + \lambda_v\mathbf{C}_m{}^{-1})^{-1}\mathbf{A}^T\mathbf{C}_e{}^{-1}\dot{\mathbf{d}} \tag{10}$$

where now the data vector $\dot{\mathbf{d}}$ is composed of successive triples of observatory orthogonal component first difference data at three consecutive months, and $\hat{\mathbf{m}}$ is our estimate of $\mathbf{m}$. $\mathbf{C}_e$ consists of 3×3 data covariance matrices for each vector data triple arranged along the diagonal, with zeroes elsewhere. $\mathbf{C}_m$ is the *a priori* model covariance matrix regularizing the flow, in this case defined by the Bloxham (1988) 'strong norm'. We investigated weaker regularizations, but the large damping parameters required to obtain converged solutions significantly over-fitted the data, and the essential features of the models were similar to those obtained using the 'strong norm'. Unconverged models fitting the data changed rapidly between epochs, lacked any coherent, large-scale structure, and the flows bore no resemblance to those obtained in other studies. We assume the field at each epoch is known, specified by the CHAOS-4 (Olsen *et al.* 2014) coefficients to degree and order 14. Various studies have investigated the effect of uncertainty in the main field on the resulting flow models. Whaler (1986) simply compared the result with two different main field models. Rygaard-Hjalsted *et al.* (2000) were the first to use a Monte Carlo Markov Chain approach, but computational resources at that time limited the applicability of the method; more recently, Baerenzung *et al.* (2014) and Baerenzung *et al.* (2016) used it to obtain a more reliable estimate of the posterior probability distribution. Lesur *et al.* (2010) adopted an iterative approach, first estimating a field model from the data, then using it to determine a starting model for the flow in the traditional fashion, and finally co-estimating the field and flow iteratively from the starting field and flow models. These studies suggest that the effect of assumptions as to the nature of the flow have at least as large an effect on the resulting flow model as any uncertainty in the main field. The SV and flow are also expanded up to degree and order

14 in eq. (8), meaning we solve for 448 flow coefficients per epoch, but because we have regularized the inversion, the results are not sensitive to this choice. We calculate the elements of **A** analytically (e.g. Whaler 1986).

Bloxham *et al.* (2002) found that a constant flow with TO superimposed provided a good fit to observatory SV; such a model requires just a few parameters. However, this conclusion was not based on an inversion of the observatory data themselves. Here, we test flow models of this type directly against the data by performing an inversion in which temporal changes in coefficients between epochs are penalized, except for the odd degree, zero order toroidal coefficients which represent TO. This involves inverting all the data simultaneously for the full time-series of flow models, that is, solving for $448 \times (n_{\mathrm{epochs}} - 2)$ coefficients, a numerically challenging computation. Consider the monthly time-series of a single flow coefficient, $m_j(i)$, $i = 1, \ldots, n_{\mathrm{epochs}}$. We construct a first difference penalty matrix that restricts time changes in m_j from month to month:

$$\mathbf{D}_j = \begin{pmatrix} 1 & -1 & 0 & \cdots & 0 \\ 0 & 1 & -1 & 0 & \cdots \\ \vdots & \vdots & \vdots & \vdots & \vdots \\ 0 & \cdots & 0 & 1 & -1 \\ 0 & \cdots & 0 & 0 & 1 \end{pmatrix} \tag{11}$$

and apply it, to all except the TO coefficients (for which the entries in $\mathbf{D}_j$ are zero), as an additional side constraint. The parameter λ_t controls how strongly the constraint is applied, resulting in an additional term $\lambda_t \mathbf{D}^T \mathbf{D}$ in the inversion (eq. 10, extended to include all data and epochs). We refer to flows obtained with this constraint as TO-like flows.

The size of this inverse problem is not amenable to direct inversion, but fortunately most elements of the enhanced normal equations matrix vanish, so iterative sparse matrix techniques are appropriate. We used the conjugate gradient algorithm with Jacobi pre-conditioning, having validated on a smaller system (with $N_{\mathrm{max}} = 8$) that the results of direct and iterative inversions agree satisfactorily.

In addition, we found the minimum amount of temporal variability required to fit monthly mean estimates of SV adequately by applying the temporal constraint, eq. (11), to all coefficients. We refer to these as minimum acceleration flows.

3 DATA

We used data from up to 128 observatories, shown in Fig. 1, between January 1997 and July 2013. Monthly means of orthogonal vector components were calculated in the traditional fashion, as the arithmetic mean of hourly mean values from all days, to give ordinary monthly means (*omm*) and using the method of Olsen *et al.* (2014), to give revised monthly means (*rmm*). *rmm* are also calculated using data from all days of a given month, but using a robust averaging procedure, and after removal of ionospheric and magnetospheric contributions. The magnetospheric ring current is characterized by a new index, *RC* (Olsen *et al.* 2014), that does not suffer from the baseline changes inherent in *Dst*. Ionospheric *Sq* was estimated using the CM4 model of Sabaka *et al.* (2004). First differences a year apart were taken to provide SV estimates, ascribed to the mid-point of the interval, giving 187 monthly data sets covering the period July 1997 to January 2013. The SV derived from the two sets of means agreed in its major features, but the *rmm* SV was less scattered than that from the *omm* (by a factor of typically 3), and also had fewer short timescale (i.e. over periods of several months) excursions. Since these excursions were only present in the *omm*, we suspect that they reflect external field contamination that was not removed when data were processed in the traditional manner. SV data covariance matrices were formed from robust estimates of the variances and cross-variances of generalized covariance function spline fits to the $\dot{X}$, $\dot{Y}$ and $\dot{Z}$ time-series, for both *omm* and *rmm*. Values of both diagonal and off-diagonal elements tended to be larger for *omm* than *rmm*. Examples of *omm* and *rmm* SV at a selection of observatories, with their standard deviations, are shown in Figs 2 and 3. Oscillations with periods of 2–3 yr are seen in some observatory mean first differences, both *omm* and *rmm* (e.g. $\dot{Y}$ at Hermanus observatory). *rmm* processing helps clean up the signals, but there is still some contamination, especially at high latitudes. Figs 2 and 3 show predictions of the CHAOS-4 model, which also exhibits some oscillations with similar periodicities. Ionospheric currents are internal to satellite data, so in principle their effects could be mapped into the internal field, and periods of 2–3 yr are easily representable with the 6-month spacing of CHAOS-4's B-spline basis. However, oscillations that are not consistent between satellite and observatory data should be suppressed as far as possible by temporal regularization, though some contamination of the internal field remains possible. Observatories suffer from the usual problem of poor geographical distribution, in particular, concentration over Europe and, to some extent, North America, and very few over the oceans and southern hemisphere (Fig. 1). We will see this reflected in the averaging functions for our core flow models in Section 4.4.

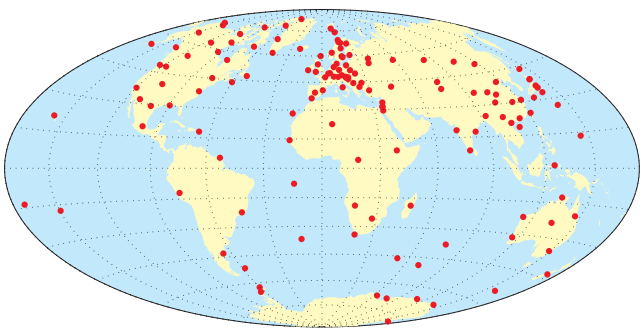

Figure 1. Observatories contributing data used in the analysis.

4 RESULTS

4.1 Original versus revised monthly mean flows

We first describe and compare the results of inverting sets of three consecutive months of SV data for flow snapshots, using eq. (10), from both *omm* and *rmm* data. We tested a variety of damping parameters λ_v to find a value for which flows converged but retained enough structure to provide a reasonable fit to the data. This value, 10^{-4}, was then fixed for all subsequent inversions, and was the same for *omm* and *rmm* inversions. The overall root-mean-square (rms) misfits for all 185 flows were 0.91 and 0.90 for *omm* and *rmm* data respectively. These are lower than the expected value of 1 because there are a number of epochs for which only a relatively small number of data are available, and these tend to be heavily over-fitted. For a more typical flow (obtained from of order 1000 data), the rms misfit was around 1.3 for *omm* and 1.1 for *rmm* inversions, and the rms flow speed was in the range 12–15 km yr^{-1}.

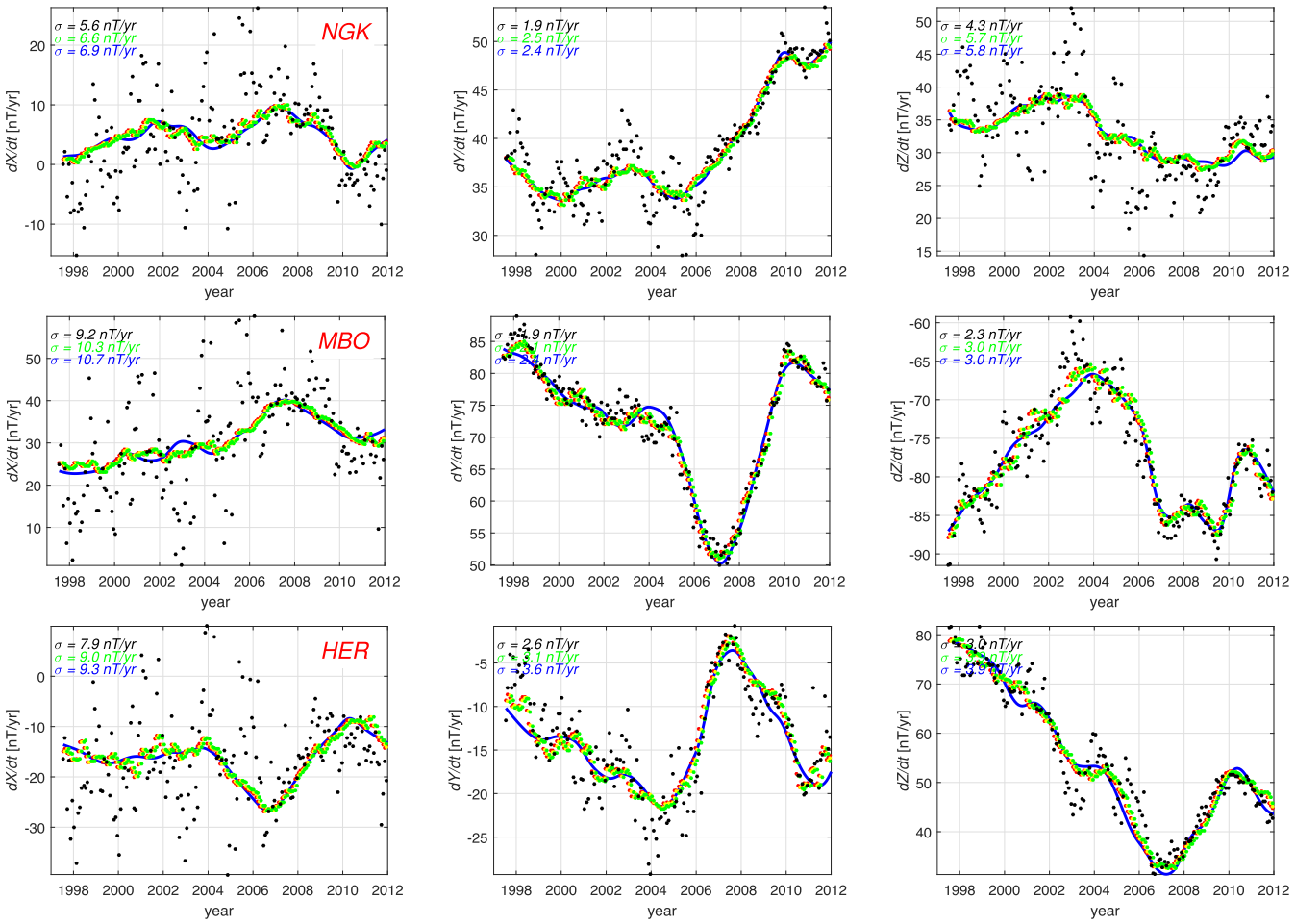

Figure 2. Time-series of *omm* SV data at Niemegk, M'Bour and Hermanus observatories (black dots) and their predictions by the flow (red, yellow and green dots when the datum is the first, second or final month of the three contributing to the flow estimation). The blue line is the prediction of CHAOS-4. Standard deviations in the top left of each panel are of a generalized covariance fit to the original data (black), from the flow predictions when it is the third month contributing to the estimate (green) and from the CHAOS-4 fit (blue). Panels are arranged $\dot{X}$, $\dot{Y}$ and $\dot{Z}$ from left to right.

We do not seek to achieve values as low as the expected misfit value of 1 because we expect there to be some diffusion which is not accounted for in these frozen-flux inversions, to allow for the SV generated by the interaction of unresolved small-scale flow and small-scale field (Eymin & Hulot 2005), and because we assume the main field is perfectly known when in fact it is subject to uncertainty. Reducing the damping parameter to bring the typical misfit down to 1 gave barely converged solutions with little coherency from epoch to epoch, especially for the *omm* flows.

The fit to the data and non-normalized standard deviations are shown in Figs 2 and 3, for a selection of observatories. The data standard deviations are up to ∼10 nT yr^{-1} for *omm*, and typically 1–2 nT yr^{-1} for *rmm*. Except at the end points, each month's SV estimates were used in three inversions (when they were the first, middle or final month of the three used); their predictions are virtually indistinguishable, especially for the *rmm* flows. The predictions are smoothly varying yet follow the rapid SV changes, such as in $\dot{Z}$ at M'Bour observatory between 2006 and 2011. They reproduce features which are not fully captured by field models in which the temporal variability is expressed using B-splines, such as the CHAOS series (e.g. Olsen *et al.* 2006, 2014), including in $\dot{Y}$ at M'Bour observatory around 2004, and in $\dot{Z}$ at Niemegk observatory from 2006 onwards, and hence their standard deviations are lower than for the CHAOS-4 model. The difference in goodness-of-fit to the *omm* and *rmm* data is clearly visible, both from the time-series and the standard deviations. The fit to each component at each observatory is broadly commensurate with the overall normalized misfits of the flow models (and so is poorer for the *omm* compared to the *rmm* data) – there is no evidence for over-fitting some components or observatories at the expense of the fit to others, or for the fit being better at, say, times of slower SV. The *omm* flows follow excursions in the data that are not seen in the *rmm*, such as in $\dot{Z}$ at Hermanus observatory between 2002 and 2004 and which are likely to be the result of external field contamination. However, the differences between the flows obtained from *omm* and *rmm* are generally rather small, and are almost impossible to discern by eye. Since the main differences between the *omm* and *rmm* SV are in features that we suspect arise from greater external field contamination in the *omm*, and because these differences do not give rise to substantially different flow models, henceforth we describe only the results obtained from *rmm*.

4.2 Temporal variability of flows

The sequence of flow snapshots undergoes some notable changes over the 16 yr investigated, particularly in the anti-clockwise eddy beneath the southern Indian Ocean, which disappears and reappears

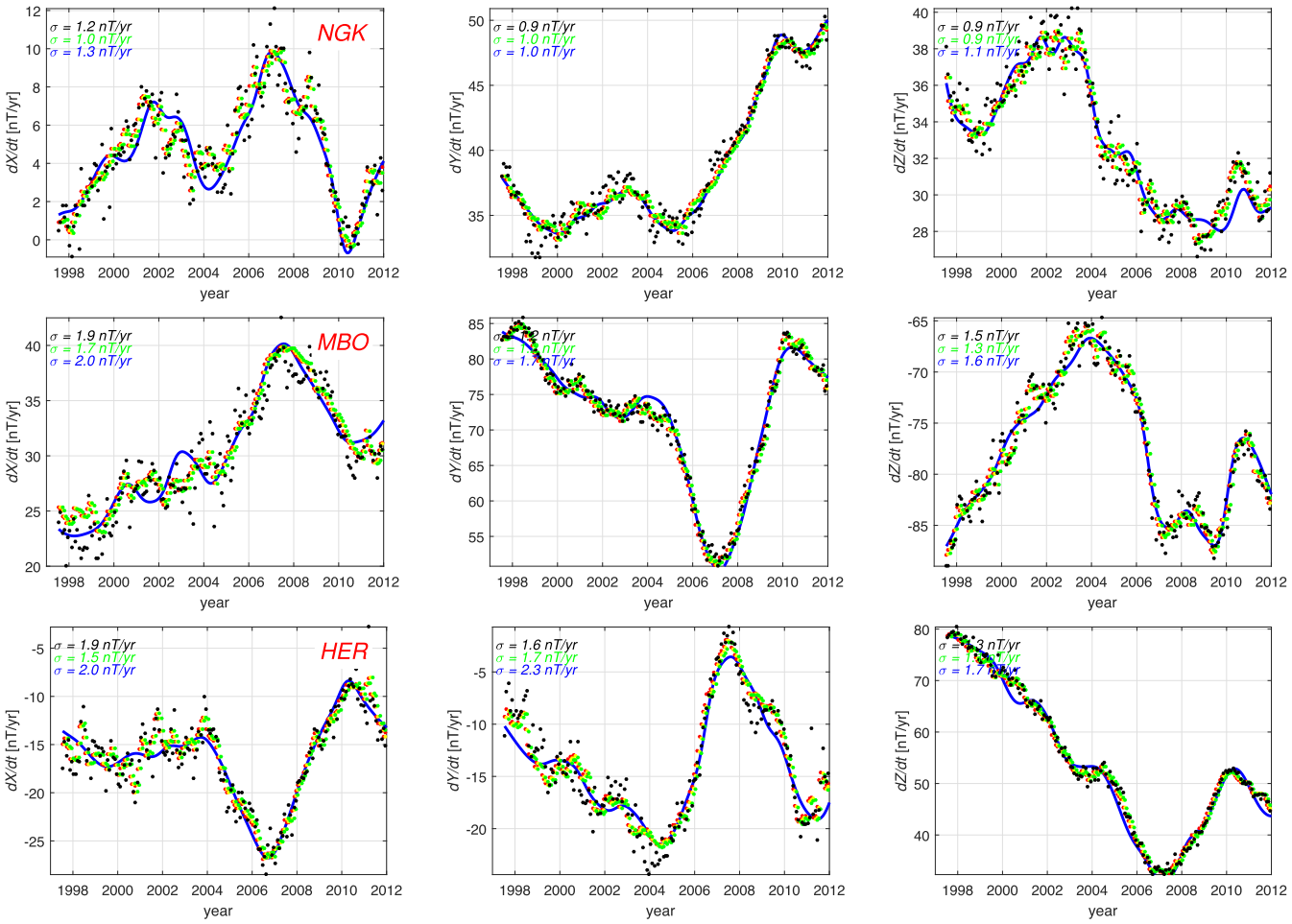

Figure 3. As for Fig. 2 but for revised monthly means, *rmm*.

twice, each time over the period of just a few months, in the first decade of the 21st century (see the Supporting Information). The eastern part of the eddy remains in place, but the western part, a southward flow, gets stretched out to the west so that the eddy is no longer closed. These changes in the flow geometry take place at times of jumps in the inter-decadal length-of-day, thought to be linked to the occurrences of geomagnetic jerks (Holme & de Viron 2013).

Decadal timescale length-of-day changes, ΔLOD, have been shown to be consistent with exchange of angular momentum between the mantle and core through the excitation of TO (Jault *et al.* 1988; Gillet *et al.* 2015). The change in angular momentum, and hence length-of-day, carried by these flows is dominated by zonal toroidal coefficients of degrees 1 and 3. Can we reduce the temporal variability of the flow, and match the observed ΔLOD, while retaining an adequate fit to the data? Since the ΔLOD are often assumed to arise through the excitation of TO-like flows, we seek flows that are constant except for motion consistent with TO by applying the penalty matrix constraint (eq. 11) to all but the TO flow coefficients, that is, except to the t_n^0 with n odd that represent toroidal, zonal and equatorially symmetric flows. For relatively small values of λ_t, the misfit is similar to that of the sequence of flow snapshots (0.92 compared to 0.90; Table 1), but with much less temporal variability in all flow coefficients, that is, including those whose temporal differences are not directly penalized. Fig. 4 shows the coefficients up to degree and order 4 as a function of time, for the flow snapshots

Table 1. Root-mean-square (rms) speed, v, of the total flow for a typical epoch, centred on October 2005, and the partitioning of its kinetic energy into the toroidal (T), poloidal (P), equatorially symmetric (S), equatorially asymmetric (AS), tangentially geostropic (TG), tangentially ageostrophic (AG) and zonal toroidal (ZT) components, expressed as a percentage. $v_{\rm rmm}$ is the flow snapshot from *rmm* data, $v_{\rm TO}$ (moderate) a TO-like flow with a temporal damping parameter λ_t of 10^3, $v_{\rm TO}$ (strong) a TO-like flow with temporal damping parameter 10^6, and $v_{\rm MA}$ a minimum acceleration flow with temporal damping parameter 10^4 applied to all flow coefficients. To make the results comparable, misfit refers to all epochs, that is, in the case of the flow snapshot in the first line, is the rms misfit over all such models.

Flow	v (km yr^{-1})	T (per cent)	P (per cent)	S (per cent)	AS (per cent)	TG (per cent)	AG (per cent)	ZT (per cent)	Misfit
$v_{\rm rmm}$	12.2	82.2	17.8	77.2	22.8	79.8	20.2	41.4	0.90
$v_{\rm TO}$ (moderate)	11.3	87.0	13.0	80.7	19.3	81.6	18.4	48.8	0.92
$v_{\rm TO}$ (strong)	10.8	86.5	13.5	79.1	20.9	80.1	19.9	48.1	1.77
$v_{\rm MA}$	11.5	88.3	11.7	81.1	18.9	82.2	17.8	55.3	0.92

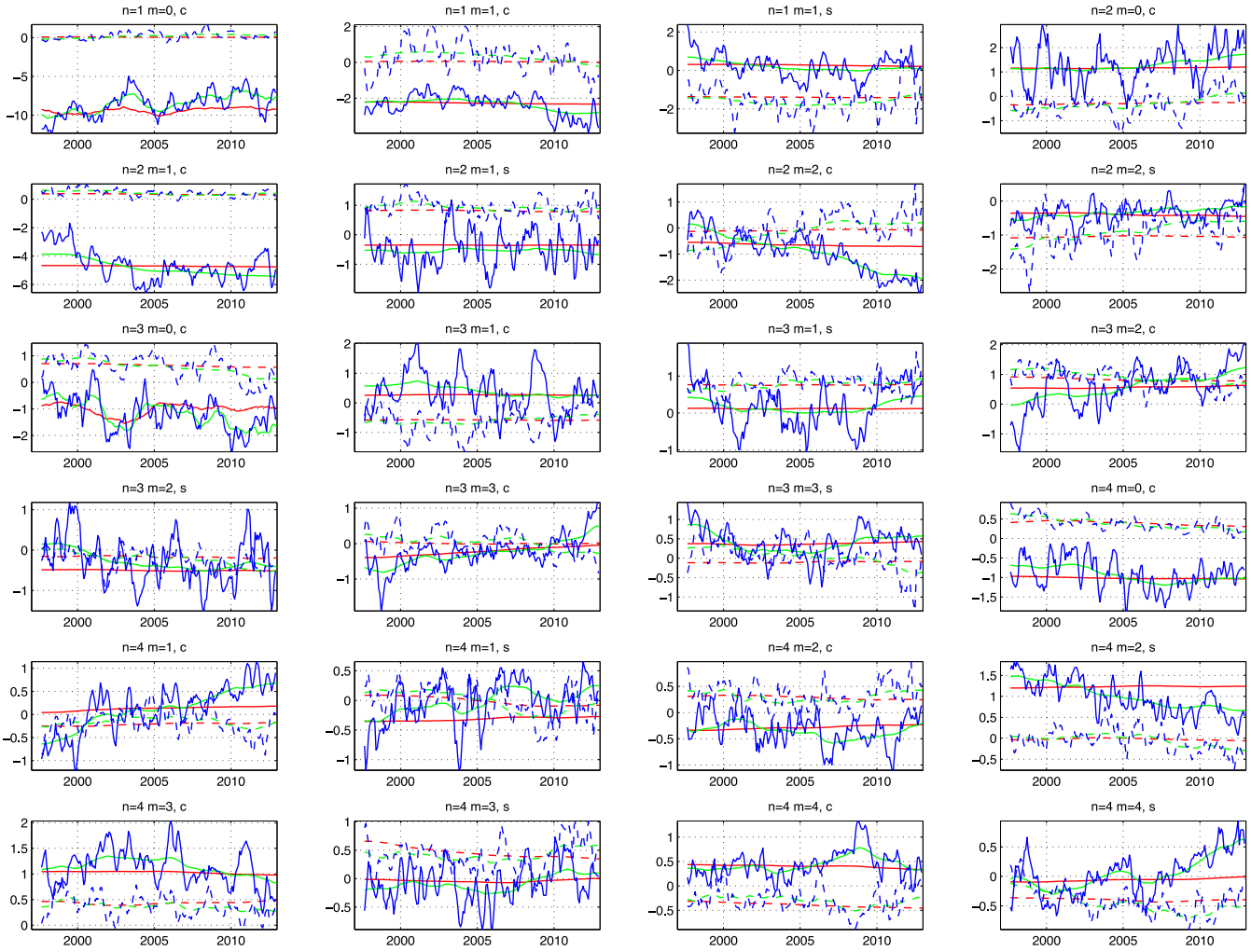

Figure 4. Temporal variability of flow coefficients (in km yr^{-1}) up to degree and order 4. Degree (n) and order (m) and whether the coefficient multiplies $\cos m\phi$ (c) or $\sin m\phi$ (s) is given above each panel. Solid lines are for toroidal coefficients, dashed lines for poloidal coefficients. Blue: flow snapshots; green: moderately TO flows; red: strongly TO flows.

(blue curves) and for such a moderately TO-like flow (green curves). There are significant differences between the two models for all coefficients, especially in the high frequencies, which are virtually absent in the constrained coefficients, and significantly reduced in those that are not directly penalized. As we increase λ_t, the misfit increases dramatically, such that when the non-TO coefficients are (essentially) steady (illustrated by the red curves in Fig. 4), it has a value of 1.77. Thus we can conclude that a constant flow with TO superimposed does not provide an adequate fit to the SV data. Similar conclusions regarding the inadequacy of TO to explain the SV have been reached by other means, for example in the studies by Wardinski *et al.* (2008), Silva & Hulot (2012) and Chulliat & Maus (2014). It is also noteworthy that TO are unable to produce changes in the axial dipole field. Sample observatory fits and standard deviations are shown in Fig. 5, from which it can be seen that such a model fails in some cases to reproduce the amplitude of the SV (e.g. $\dot{X}$ at Hermanus around 2007, and $\dot{Y}$ at M'Bour around 2010) and in others does not predict the correct amount of variability (especially in $\dot{X}$ e.g. from 2000 at Canberra). The standard deviations of the moderately TO-like flow are very similar to those of the sequence of flow snapshots, but in general are markedly higher for the steady flow with TO superimposed.

Although we have demonstrated that flows that are steady except for TO do not provide an adequate fit to the data, we have also shown that flows need relatively little temporal variability to be able to reproduce quite rapid SV in individual observatory components. Thus the time changes found in the sequence of flow snapshots is not required to fit the data. To establish the minimum amount of temporal variability necessary to explain the data, we penalized all flow coefficients using eq. (11), varying the temporal damping parameter λ_t until the misfit matched the value obtained for the moderately TO-like flow (Table 1). For these minimum acceleration flows, it is difficult to discern any temporal flow changes by eye (see the Supporting Information), but inspection of the differences from the mean demonstrates that the largest changes are in the equatorial and southern hemisphere regions in a band around 90° wide centred on 180° longitude (see the Supporting Information).

Restricting the temporal variability of the flows, either to produce TO-like or minimum acceleration flows, does not change their basic geometry (see the Supporting Information), and they remain predominantly toroidal, equatorially symmetric, tangentially geostrophic, and with a significant zonal toroidal component (Table 1).

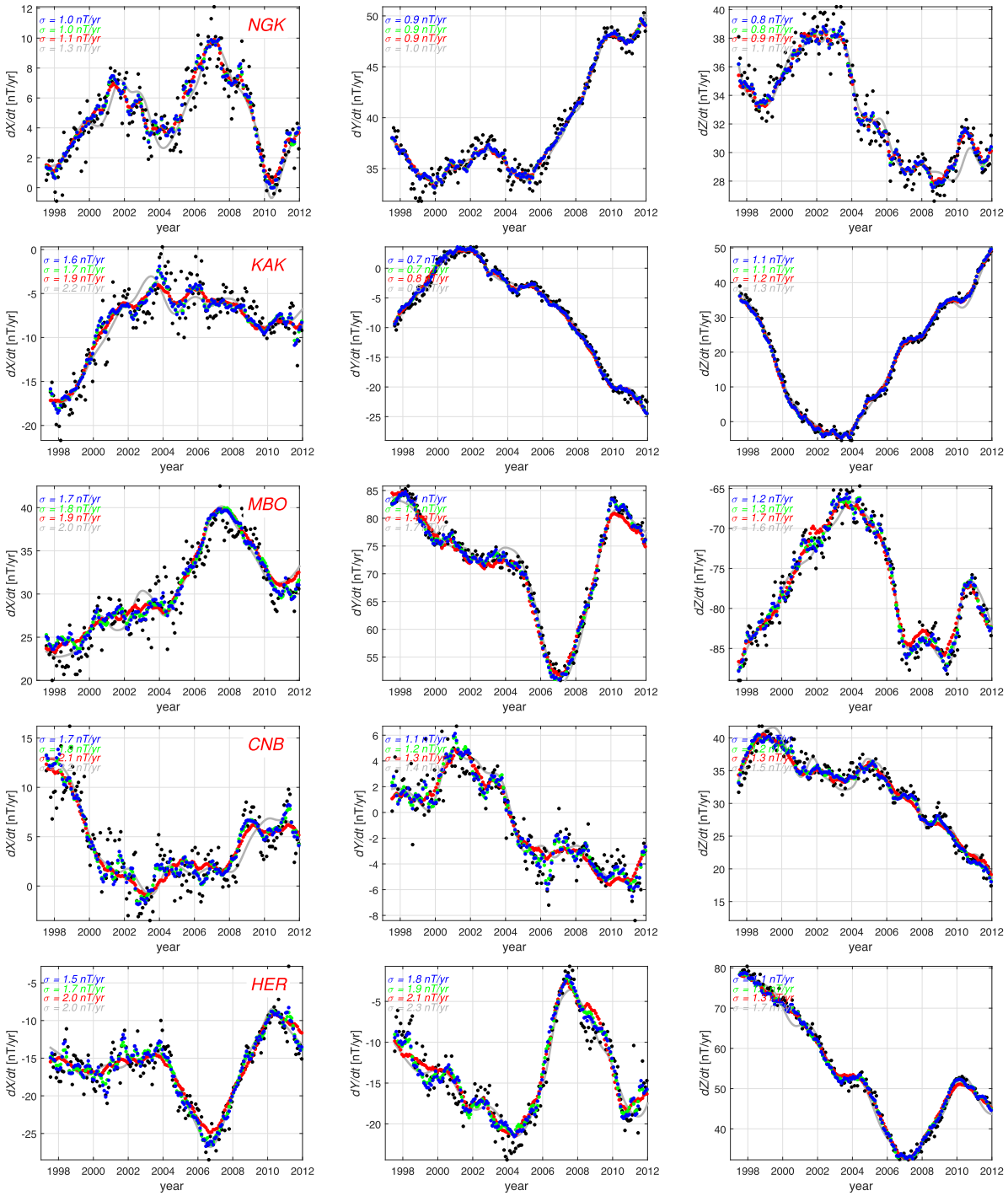

Figure 5. Data (black dots) and their predictions by flow models at Niemegk, Kakioka, M'Bour, Canberra and Hermanus observatories. Blue: flow snapshots; green: moderately TO flows; red: strongly TO flows. The grey line is the prediction of CHAOS-4. Standard deviations in the top left of each panel have the same colour codings.

4.3 Resolution

Two ways to assess how well the flows are resolved are through resolution matrices of the flow coefficients, and averaging functions derived from them that indicate the extent of spatial averaging to form a flow estimate at a given point on the CMB. The resolution matrix is (e.g. Bloxham *et al.* 1989)

$$\mathbf{R} = (\mathbf{A}^T \mathbf{C}_e{}^{-1} \mathbf{A} + \lambda_v \mathbf{C}_m{}^{-1})^{-1} \mathbf{A}^T \mathbf{C}_e{}^{-1} \mathbf{A} \qquad (12)$$

extended to include a term involving the second damping parameter λ_t if the temporal side constraint (eq. 11) is also imposed. $\mathbf{R}$ relates the estimated parameters ($\hat{\mathbf{m}}$) to their true values ($\mathbf{m}$), and therefore the ideal resolution matrix is the identity matrix. Although an un-regularized solution has perfect resolution (if there are more data than model parameters, as is the case for most epochs of the period we studied), other aspects of such models are undesirable, such as the lack of convergence of the power spectra, meaning that the values of many of the coefficients change substantially if

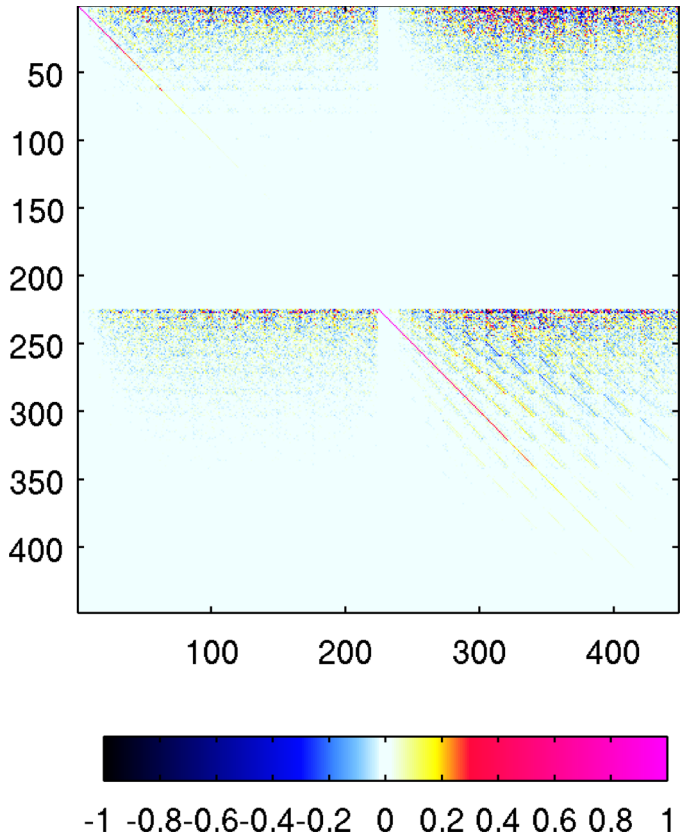

Figure 6. Resolution matrix for the flow snapshot centred on October 2005. Toroidal flow coefficients are numbers 1 to 224, and poloidal coefficients from 225 to 448.

the spherical harmonic limit N_{max} of the flow coefficients changes. Non-zero off-diagonal elements of **R** indicate that flow coefficients are correlated, and diagonal elements deviating from 1 show that coefficient amplitudes are not correctly recovered. A typical resolution matrix for a flow snapshot is shown in Fig. 6. The significant off-diagonal elements show that estimates of individual coefficients are severely contaminated, at all spherical harmonic degrees, and not just by coefficients of the same given degree, nor just by either other toroidal or other poloidal coefficients. These correlations are more pronounced for toroidal coefficients and, in particular, estimates of the low degree and order toroidal coefficients are severely contaminated by poloidal coefficients. The diagonal elements corresponding to toroidal coefficients decrease rapidly with spherical harmonic degree and only coefficients up to degree and order 3 or so can be regarded as resolved. For a given degree (except 1), the tesseral harmonics are better resolved than the zonal ones. This is similar to the situation Bloxham *et al.* (1989) found for their historical magnetic field models which were dominated by declination data, although it is not clear why it applies to toroidal flow coefficients derived from orthogonal component observatory SV data. The decay along the diagonal is a lot more gentle for poloidal coefficients, and those up to degree and order 8 can be regarded as reasonably well resolved; similarly, the amplitude of the off-diagonal elements associated with a given poloidal coefficient tends to be smaller than for the corresponding toroidal coefficient. Previous studies also found better resolution of poloidal than toroidal flow coefficients, when calculated from both observatory SV data (Madden & Le Mouël 1982) and from spherical harmonic SV coefficients (Gire *et al.* 1986). A number of off-diagonal elements exceed 1 in absolute value, indicating very high correlations/anti-correlations between coefficients. Bloxham *et al.* (1989) found the same phenomenon in the resolution matrix for their model of the CMB radial field in epoch 1715, which was based on directional (declination and inclination) data only. The trace of the resolution matrix indicates the number of free parameters of the solution; this is typically 100 for our flows, consistent with resolution up to spherical harmonic degree approximately 6 if both toroidal and poloidal coefficients were equally well resolved. Given that most of the energy is in the toroidal flow (Table 1), it is unfortunate that its resolution is considerably poorer.

A diagonal block and its two adjacent blocks in the same row of the 82 880 × 82 880 resolution matrix for the inversion spanning all epochs with a moderately TO-like flow (i.e. with a misfit comparable to that of the individual flows), again calculated using the Jacobi pre-conditioned conjugate gradient algorithm, are shown in Fig. 7. Each block has dimension the number of flow coefficients for a given epoch, so the image indicates correlations between them, and their correlations with those from the previous and subsequent month. The structure of the diagonal block is similar to that of Fig. 6, but the diagonal elements have smaller values, that is, are less well resolved. The off-diagonal blocks have prominent diagonal elements (except for those corresponding to the odd-degree, zero order toroidal coefficients), indicating correlations between the same coefficient at successive epochs introduced through the temporal constraint, but their off-diagonal elements generally are very small. The pattern repeats for blocks further away from the diagonal but with the magnitudes of the elements decreasing. The trace of

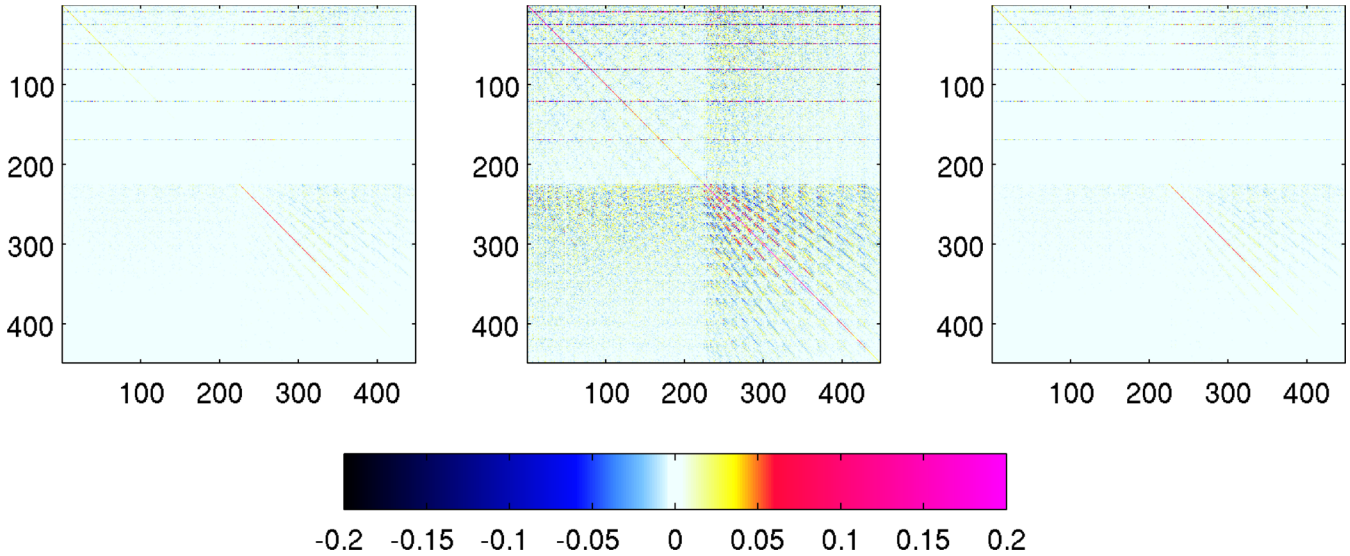

Figure 7. The diagonal block and two adjacent blocks (row-wise) of the resolution matrix for the moderately TO-like flow for October 2005. Note the different colour scale from Fig. 6.

the full 82 880 × 82 880 matrix is 9622, that is, the model resolves of order 52 coefficients, or up to degree and order 4, per epoch on average. The loss of resolution compared to the snapshot solutions is partly because of the correlations introduced by the temporal constraint; however, the trace of each immediate off-diagonal block shown in Fig. 7 is 10, which does not match the difference between the trace of the diagonal block and the trace of the resolution matrix of the snapshot solution.

In both snapshot and temporally constrained flow resolution matrices, the rows corresponding to coefficients t_n^0 with n odd stand out through having significant non-zero elements (Figs 6 and 7). This presumably reflects the null space of the flow, which depends on the geometry of the magnetic field. For example, the westward drift term represented by t_1^0 acting on an axial dipole magnetic field generates no SV. Since the axial dipole is the dominant part of the field, theoretically this flow coefficient is poorly resolved (Madden & Le Mouël 1982).

4.4 Averaging functions

Averaging functions are continuous functions of position that indicate how well a model estimate at a given point is localized. The estimated model value $\hat{m}$ is a spatial average of the true model, m, weighted (in an integral sense) by the averaging function. Here, we are interested in models defined on a spherical surface, specifically, the CMB. Hence we write

$$\hat{m}(\theta_0, \phi_0) = \oint_{\mathrm{CMB}} A(\theta_0, \phi_0, \theta, \phi) m(\theta, \phi) \mathrm{d}\Omega, \tag{13}$$

where A is a function that we would like to be well-peaked at (θ_0, ϕ_0) and small elsewhere, enclosing an area of 1 on the unit sphere. The ideal averaging function would be $\delta(\theta - \theta_0)\delta(\phi - \phi_0)$ where δ is the Dirac delta-function, since in that case, the model estimate would equal the true model. However, approximations to the ideal from finite quantities of inaccurate data are less well-peaked, may not be centred on the point of interest, and may have side lobes ('ringing' or Gibbs' phenomenon). The 2-D width, or aperture, of an averaging function indicates the area over which the point model estimate is an average of the true model, and the height of its peak indicates how reliable its amplitude is. Minimizing in a least-squares sense the difference between the averaging function and $\delta(\theta - \theta_0)\delta(\phi - \phi_0)$, Whaler & Gubbins (1981) show that the best approximation to the ideal averaging function (i.e. when the solution is not regularized, and hence resolution is perfect) for the radial magnetic field at the CMB, expressed as a finite spherical harmonic sum to degree and order N is

$$\frac{1}{4\pi} \sum_{n=1}^{N} (2n+1) P_n(\mu) \tag{14}$$

where μ is the cosine of the angle subtended at the Earth's centre between (θ_0, ϕ_0) and the point at which it is calculated. An example for $N = 14$ is given in the top row of Fig. 8, indicating that the model value at a given point is an estimate over an area subtended by an angle at the Earth's centre of at least 30°. As N increases, the central peak becomes taller and narrower, but there are always side lobes, increasing in number but decreasing in amplitude, and a small peak at the antipodal point. Hence an estimate of the CMB radial field at a given point is significantly contaminated by its value elsewhere on the core surface even in the ideal case; the contamination is worse for a regularized inversion. The same development as Whaler & Gubbins (1981) used for the CMB radial magnetic field applies to any quantity that can be expressed as a linear combination of spherical harmonics, and hence to the toroidal and poloidal scalars of the flow, $\mathcal{T}$ and $\mathcal{S}$, for which, following the notation of Bloxham *et al.* (1989), the averaging function can be written

$$A(\theta_0, \phi_0, \theta, \phi) = \mathbf{c}^{\mathrm{T}}(\theta_0, \phi_0)\mathbf{R}\mathbf{b}(\theta, \phi) \tag{15}$$

where $\mathbf{c}$ has elements of the form

$$r_c P_n^m(\cos\theta_0) \begin{Bmatrix} \cos m\phi_0 \\ \sin m\phi_0 \end{Bmatrix}$$

with r_c the core radius, and $\mathbf{b}$ has elements of the form

$$\frac{2n+1}{4\pi r_c} P_n^m(\cos\theta) \begin{Bmatrix} \cos m\phi \\ \sin m\phi \end{Bmatrix}.$$

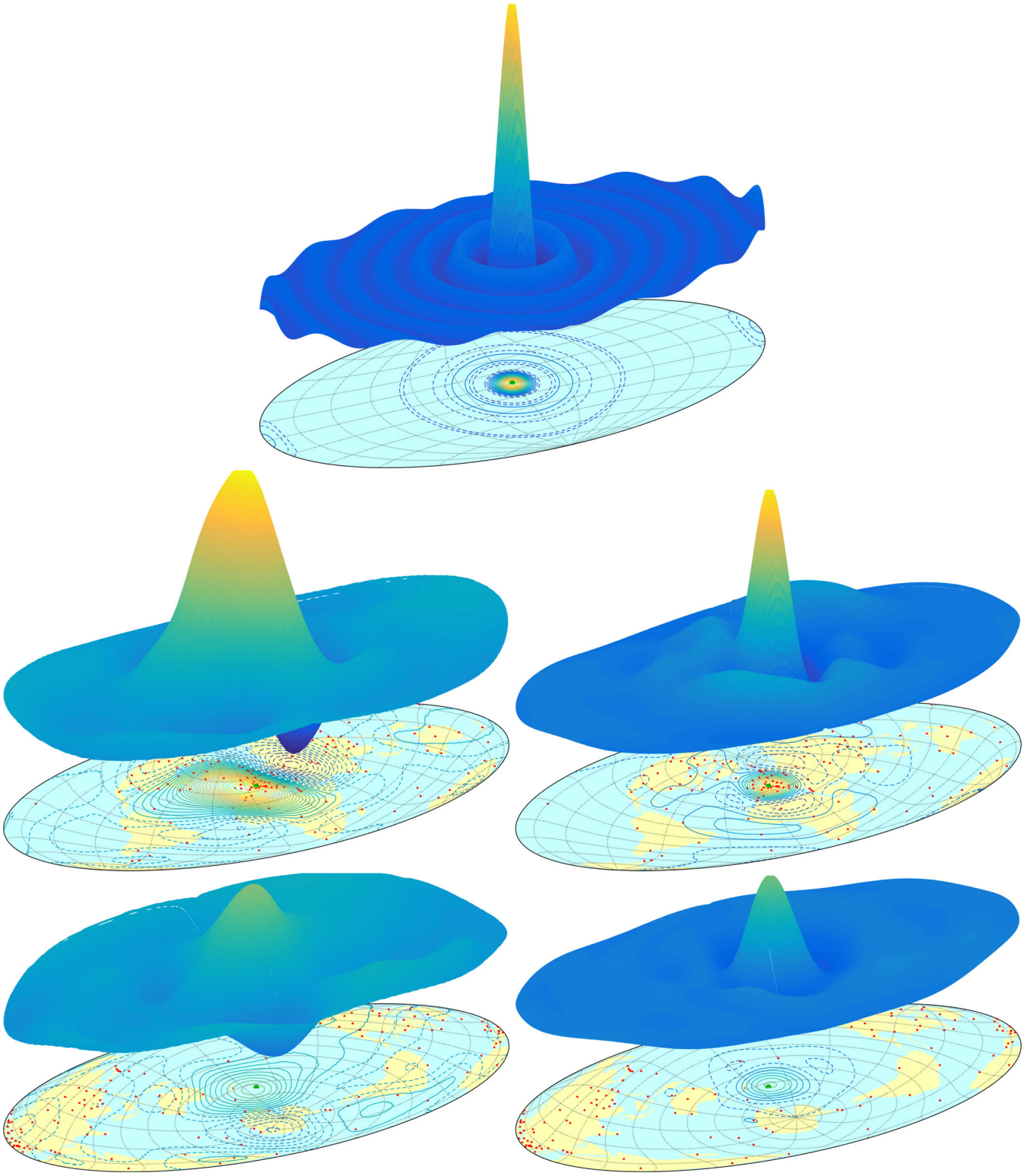

Figure 8. Averaging functions for toroidal and poloidal flow scalars. Top: best approximation to the ideal averaging function for flows to degree and order 14; it is independent of location. Middle: actual averaging functions for the toroidal (left) and poloidal (right) scalars at (50°N, 10°E) for a typical spatially regularized flow. Bottom: as for the middle panel, but at (50°S, 170°W). The green dot on the map projection marks the point at which the averaging function is centred. Contour interval is 1 for the ideal and poloidal flow scalar averaging functions, 0.1 for the toroidal scalar averaging functions, with negative contours dashed.

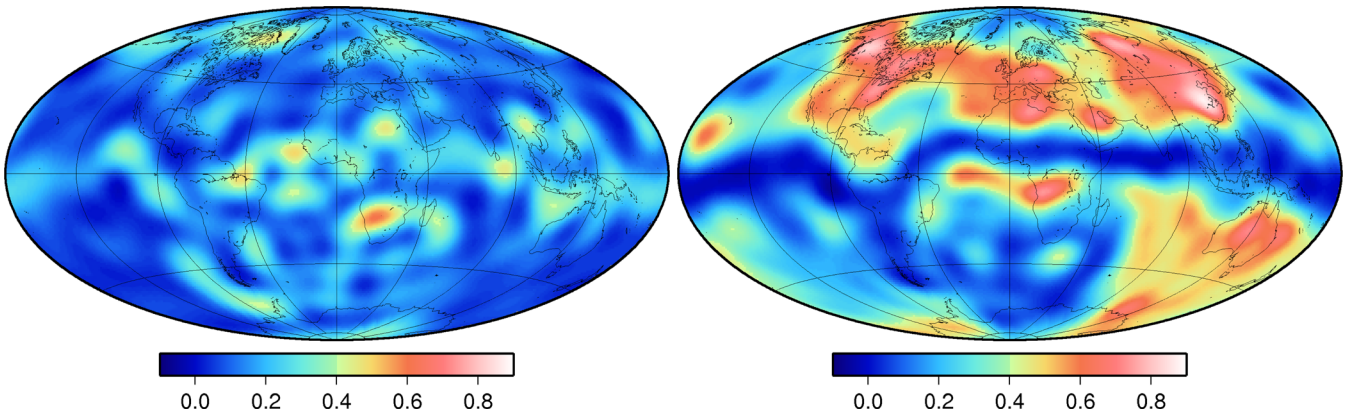

Figure 9. Averaging function at the point at which it is centred as a fraction of the maximum possible value for a typical epoch, for the toroidal (left) and poloidal (right) scalars. Continents shown for reference.

Using the addition theorem for spherical harmonics, eq. (14) is recovered if resolution is perfect ($\mathbf{R} = \mathbf{I}$). In the Appendix, we discuss efforts to form averaging functions for the flow components themselves, which are combinations of derivatives of the spherical harmonics, rather than of spherical harmonics themselves.

The middle row of Fig. 8 shows the comparison at the same scale for the averaging functions for the toroidal (left) and poloidal (right) flow scalars centred on (50°N, 10°E) where the high concentration of European observatories should provide good flow resolution, for a typical flow snapshot. However, the averaging functions are poorly peaked, broad and can reach amplitudes comparable to those at the point at which they are centred elsewhere on the CMB. The toroidal scalar averaging function is a much poorer approximation to the ideal than that for the poloidal scalar, in agreement with the evidence from the resolution matrix. The bottom row of Fig. 8 shows the same averaging functions centred on (50°S, 170°W) where, as expected, the low density of observatories provides even poorer resolution. Here, the toroidal flow is essentially unresolved – the averaging function has only a weak maximum at the point at which it is centred. With central peak widths of at least 50° for the toroidal part, flow features such as the anti-clockwise eddy beneath the southern Indian Ocean are barely resolved.

To capture the global variability in the toroidal and poloidal scalar averaging functions, Fig. 9 plots them at the point they are centred as a fraction of the maximum possible value from a truncated spherical harmonic sum (given by eq. 14 with $\mu = 1$). Over large parts of the CMB, the toroidal scalar averaging function is no more than about 20 per cent of its maximum possible value, and never exceeds 60 per cent of it. These low values are a combination of generally poor resolution and the averaging function peaking in the 'wrong' place, that is, not at the point at which it is centred. The distribution of the poloidal scalar averaging function is more variable. Over large areas of the northern hemisphere continental land masses where there observatories are concentrated (Fig. 1) it exceeds 60 per cent and approaches 90 per cent of the maximum possible value. However, there is a pronounced band of very low values around the magnetic equator, extending into the large areas of reverse flux in the southern hemisphere beneath South America, the Atlantic region and southern Africa. This is reminiscent of the areas affected by the 'Backus effect' in main field modelling of scalar data. We noted above that the resolution matrix contains features that Bloxham *et al.* (1989) associated with ambiguity in magnetic field modelling based on only directional data (e.g. off-diagonal elements with magnitude greater than 1). Methods of analysing this ambiguity (e.g. Gubbins & Proctor 1990; Hulot *et al.* 1997) cannot obviously be applied to core flow modelling. We suggest that it reflects a null-space of the poloidal flow component, one that is similar to, but different from, the ambiguous regions for tangentially geostrophic flows, which are connected to the geographic, rather than magnetic, equator. There are patches of the CMB where the toroidal and poloidal scalar averaging functions are negative at the point at which they are centred, meaning that the estimate there, rather than being dominated by the actual flow, has a negative contribution from it. Regardless of location on the CMB, we find that the flow, especially its toroidal component, is not well resolved by ground observatory data.

The resolution matrix and averaging functions depend on the data distribution and the value(s) of the damping parameter(s), which are varied according to the quality and quantity of data available. Assuming the flow is constant over a period longer than three months might improve its spatial resolution (as measured by the averaging function) because of the increased quantity of data, but this would be at the expense of poorer temporal resolution. Similarly, an increased data density, such as that provided by satellite data, should improve the resolution and averaging functions; however, we cannot predict by how much, nor whether a more even data distribution would reduce the correlations between (in particular) toroidal flow coefficients, partly because this will depend on the specific damping applied.

5 DISCUSSION

Our flows exhibit the main features of many previously published models, such as having a strong band of westward flow in the equatorial region in the hemisphere centred on the Greenwich meridian, slower flow beneath the Pacific, and an anti-clockwise eddy beneath the southern Indian Ocean at most epochs (see Holme 2015). They are less equatorially symmetric than flows derived under the quasi-geostrophic constraint (Pais & Jault 2008), and have weaker sub-Pacific flow than most derived under the assumption that the flow is tangentially geostrophic. However, they are predominantly toroidal, equatorially symmetric and tangentially geostrophic, and have a substantial zonal toroidal component (Table 1). An example snapshot flow and its power spectra are shown in Fig. 10. The time-average of the flow snapshots and the averages of those which have been temporally constrained are indistinguishably different by eye, and closely resemble that shown in Fig. 10. Like the

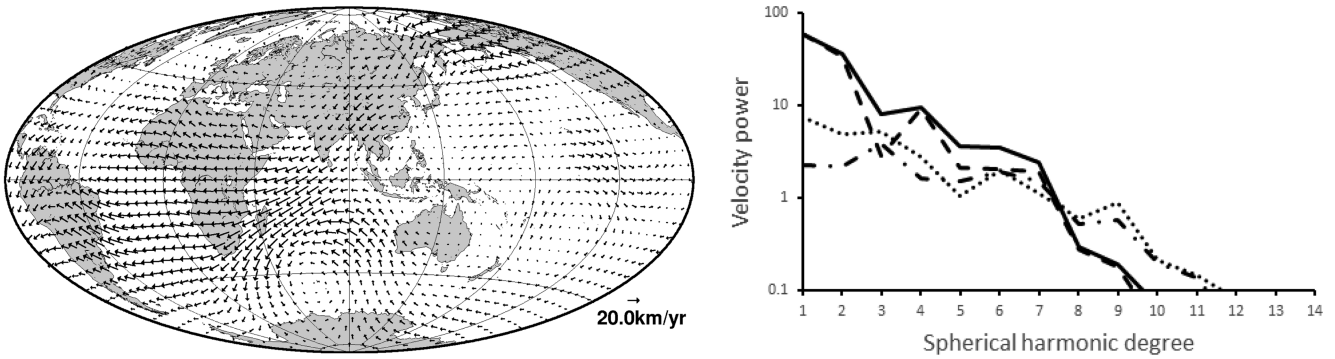

Figure 10. Left: CMB flow (at a typical epoch, centred on October 2005) from inverting three consecutive months of *rmm* first difference data. Continents shown for reference. Right: flow power spectra, units $(\mathrm{km\,yr^{-1}})^2$. Solid and dotted lines are power in the toroidal and poloidal components, respectively, of the flow in the left panel. Dashed and dot-dashed lines are the corresponding power spectra of the moderately TO-like flow.

individual epoch flows, they are predominantly toroidal, tangentially geostrophic, equatorially symmetric and zonal toroidal. These time-average flows, which account for much of the data variance, are large scale and simple. Flows deduced from satellite data, or spherical harmonic models derived from them, generally show more detail, but we can see evidence in our flows for more diffuse expressions of their features. For example, our flows have a northward component beneath North America, westward flow beneath the northern-post Pacific Ocean and a southward component beneath eastern Asia which, if focussed, would form part of the eccentric planetary gyre characteristic of quasi-geostrophic flows discussed by Gillet *et al.* (2009), amongst others. This feature of our flow resembles more closely that of Baerenzung *et al.* (2014) which, although derived from satellite data, has a less spatially concentrated gyre. Baerenzung *et al.* (2016) note that it is not necessary to make the quasi-geostrophic assumption to obtain flows with an eccentric planetary gyre. Similarly, in the southern hemisphere, northward flow around 90°E, westward flow beneath the Atlantic Ocean, then turning south, is seen in models derived from satellite data (e.g. Holme & Olsen 2006; Silva & Hulot 2012; Lesur *et al.* 2015; Baerenzung *et al.* 2016). The strong southward flow beneath the western Indian Ocean visible in Fig. 10, completing the anti-clockwise eddy, is not, or is only weakly, present in most satellite data-based flows. Similarly, the small clockwise eddy beneath the south-western Pacific Ocean is not generally a feature of models derived from satellite data – in fact, the tangentially geostrophic flow of Holme & Olsen (2006) has a weak clockwise eddy, but their toroidal flow has an anti-clockwise eddy in the same location (and, as noted above, features of this size are not well resolved by observatory data). Besides generally decreasing power spectra for both toroidal and poloidal flow components, and an approximately order-of-magnitude difference between the toroidal and poloidal power, the dominant feature of the spectra is the loss of power at toroidal degree 3 (e.g. Holme & Olsen 2006; Lesur *et al.* 2010, 2015; Baerenzung *et al.* 2014, 2016), regardless of whether or not the flow is assumed tangentially geostrophic. All these features are present in our spectra, for both snapshot and moderately TO-like flows (Fig. 10). The flow of Baerenzung *et al.* (2016) with highest posterior probability density is faster than ours but similar in morphology, though again with more localized features; its toroidal power spectrum has a similar shape to ours, but its poloidal spectrum is markedly different at low harmonic degree, as it increases with increasing degree.

While the basic features of the time-average flow do not depend on what type of flow is sought, the fluctuations around it are very different, depending mainly on whether or not a temporal constraint is applied. As noted previously, these fluctuations can be quite substantial for snapshot flows, including a change to the morphology of the flow beneath the Indian Ocean, specifically, that it does not remain as a closed eddy throughout. This region is unusual in that, when temporal variability is restricted by seeking a moderately TO-like flow, the fluctuations in its upwelling and downwelling remain. The time-average flow has an upwelling beneath the eastern part of the Indian Ocean, and a downwelling beneath the western part, similar to the pattern seen in the flows Olsen & Mandea (2008) generated for 2003–2004 to fit rapid changes in the SV. From mid-2004, these over-turning features of our temporally constrained flows start to weaken. In contrast, the downwellings beneath northern South America and the northern Pacific Ocean, and the upwelling beneath Hawaii, remain in place throughout the period of our study. In general, the fluctuating part of the flow has a higher proportion of its kinetic energy in the poloidal component than the average flow (typically ∼35 per cent for epochs of the moderately TO-like flow, higher for flow snapshots, compared to ≤20 per cent for the time-average part). Beneath the equatorial western Pacific, the fluctuations in the moderately TO-like flow model are dominated by the toroidal component, changing steadily by an anti-clockwise rotation superimposed on a strengthening westward zonal flow. Fig. 2A of Finlay & Jackson (2003) shows that the historical field evolution is consistent with waves propagating westward away from this location. Beneath the western Atlantic and eastern Americas, the fluctuations show an increasing southward component to the flow (deviations from the mean are predominantly northward at the beginning of the interval and finish predominantly southward, with a weak anti-clockwise rotation).

Although the TO-like flow changes slowly throughout the interval modelled, there are rapid changes and local variability in fluid acceleration which, in order to reduce noise, we have estimated by fitting smoothing splines to the discrete monthly flow coefficients and then differentiating the spline representation. For example, in the equatorial region beneath the western Atlantic and eastern Americas there are peaks in a predominantly poloidal acceleration of opposite sign in 2006 and 2009, the times at which Chulliat & Maus (2014) note an anti-correlated pulse in CMB secular acceleration there. They also found that a constant flow and TO (with an assumed 6 yr period) did not provide an adequate fit to secular acceleration data. Our fluid acceleration power has maxima in 2007 and 2009.5 (and also in 2000, 2002 and 2003.5); the variability has an amplitude of about 0.5 $(\mathrm{km\,yr^{-2}})^2$ around a mean of ∼3 $(\mathrm{km\,yr^{-2}})^2$.

Fig. 11 shows the temporal variability of the non-zonal part of v_ϕ at 85°W; at the equator, it undergoes a sign change in around

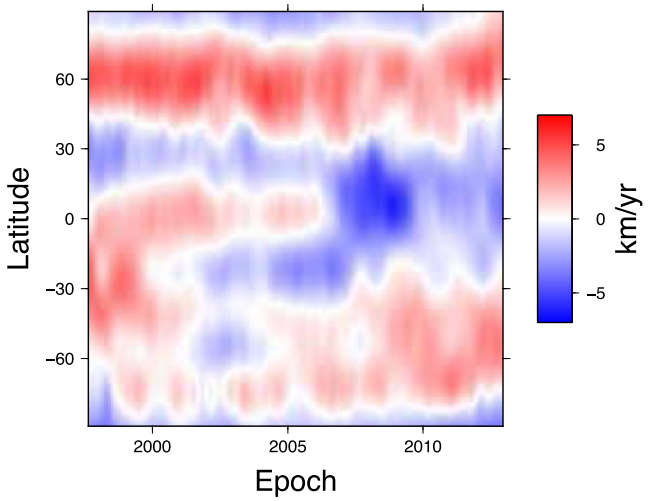

Figure 11. The non-zonal component of v_ϕ of the moderately TO-like flow at 85°W as a function of latitude and time.

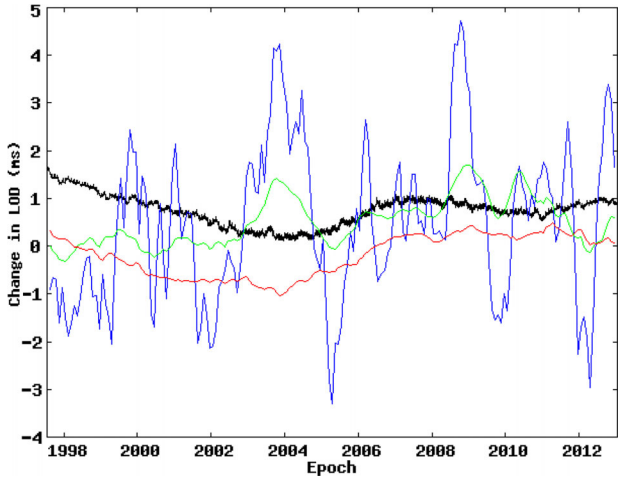

Figure 12. Change in LOD and its prediction by flows. The data (black curve) have been corrected for atmospheric effects, the annual and semi-annual signals removed and then a moving average over 31 d was taken. The predictions of the flows use the same colour coding as Figs 4 and 5, that is, blue: flow snapshots, green: moderately TO and red: strongly TO. The curves have been offset for clarity.

2006 followed by a pulse of westward flow until 2009 when it weakens again. Such temporal variability is another indicator that zonal TO superimposed on a steady flow are insufficient to fit the data. Over most of the core surface, non-zonal v_ϕ is faster and more-or-less steady; it is also much more equatorially symmetric at 85°W than at other longitudes. At the same location, the non-zonal v_ϕ of Gillet *et al.* (2015) undergoes a series of oscillations with a period of about 7 yr (see their fig. 12). They also report a minimum in amplitude at 10° latitude, but their flows are equatorially symmetric under the quasi-geostrophic constraint; typically, non-zonal v_ϕ of our moderately TO-like flow is strongly asymmetric about the equator. Beneath the Asian land mass the flow also shows strong deviations from the mean, which is dominated by a southward jet feeding into the band of equatorial westward flow.

None of our models that fit the data adequately provides a good match to decadal ΔLOD (Fig. 12); in particular, the unconstrained flows have much shorter timescale changes, and amplitudes are a factor ∼10 too high. Wardinski (2004) and Gillet *et al.* (2015) note that excess variability (both temporally and amplitude) can result from ignoring data time covariances, as we have done here. ΔLOD predictions by the moderately TO-like and minimum acceleration flows appear to be an increasingly damped version of the unconstrained flow predictions, such that the moderately TO-like flow predicts changes of the right amplitude and with a similar amount of temporal variability, but not correlated with the ΔLOD data. In contrast, our strongly TO-like flow model forces all the flow-time-dependence into coefficients which participate in angular momentum exchanges and predicts a much better match to the observed ΔLOD, although it does not fit the SV data. We have not attempted a joint inversion of SV and ΔLOD data to establish whether there is a flow model that fits both data sets, although Holme (2015) showed that small modifications to the flow can change angular momentum predictions by a significant amount. Nor have we attempted to establish whether the much smaller inter-annual changes occurring at times of geomagnetic jerks (Holme & de Viron 2013) are reproduced by any of our models, since the uncertainties in the predictions are expected to exceed the signal. However, we did note that the substantial changes in geometry in the sequence of flow snapshots occurred at times of geomagnetic impulses.

6 CONCLUSIONS

The traditional method of calculating observatory monthly means provides estimates of SV that are more scattered than with the revised method proposed by Olsen *et al.* (2014), and they almost certainly retain some external field contamination. These features can be modelled by CMB flows that will therefore contain artefacts. We recommend that monthly means are calculated using the revised method.

By inverting SV data directly for CMB flow snapshots (assuming the main field is perfectly known), we have been able to find flows fitting the data adequately. The fit is better than that achieved by the CHAOS-4 model. These flows demonstrate rapid, but systematic, changes in geometry. The eddy beneath the Indian Ocean undergoes the most obvious change, to the extent that for part of the period studied, it is no longer closed on its western side; its strength is also rather variable. However, by restricting the month-to-month variability of the flow coefficients, we were able to provide an equally good fit to the data with considerably smaller changes in the flow. The temporally variable part of the flow must include more terms than the odd order, zero degree toroidal flow coefficients that describe TO. The more rapid changes in these flows are at times when and are located on patches of the CMB where pulses of secular acceleration occurred.

The uneven and relatively sparse observatory distribution means that the resolution of our flows is not good, as evidenced by both the resolution matrix and averaging functions. The resolution of the toroidal part of the flow, which contains about 90 per cent of the flow energy, is considerably worse than that of the poloidal part. As expected, the averaging functions are poorer approximations to the ideal beneath areas of lower observatory density at the surface, such as the Pacific Ocean. We have the prospect of improving resolution and the averaging functions from the higher density of coverage based on satellite data, such as from the current Swarm satellite constellation mission. However, the problem of external field contamination is more severe than for ground observatories, and previous estimates of point SV values from 'virtual observatories' from single satellites also appear to contain artefacts from the orbit sampling of the volume containing each virtual observatory (Beggan *et al.* 2009; Shore 2013).

ACKNOWLEDGEMENTS

This research was begun while Nils Olsen was on sabbatical at the University of Edinburgh, funded by the Leverhulme Trust. Magi Hagdorn helped with several of the computing issues. We thank two reviewers for their constructive comments. One reviewer pointed out the previous derivation of our eq. (A.7) by Winch *et al.* (2005), and suggested investigating the global variability of the averaging function that led us to produce Fig. 9, which indicates a practical null-space in the poloidal flow.

REFERENCES

Backus, G.E., 1968. Kinematics of geomagnetic secular variation in a perfectly conducting core, *Phil. Trans. R. Soc. Lond., A,* **263,** 239–266.

Baerenzung, J., Holschneider, M. & Lesur, V., 2014. Bayesian inversion for the filtered flow at the Earth's core-mantle boundary, *J. geophys. Res.,* **119**(4), 2695–2720.

Baerenzung, J., Holschneider, M. & Lesur, V., 2016. The flow at the Earth's core-mantle boundary under weak prior constraints, *J. geophys. Res.,* **121,** 1343–1364.

Beggan, C.D., Whaler, K.A. & Macmillan, S., 2009. Core flow modelling from satellite-derived 'virtual observatories', *Geophys. J. Int.,* **177,** 463–475.

Bloxham, J., 1988. The determination of fluid flow at the core surface from geomagnetic observations, in *Mathematical Geophysics, A Survey of Recent Developments in Seismology and Geodynamics,* pp. 189–208, eds Vlaar, N.J., Nolet, G., Wortel, M.J.R. & Cloetingh, S.A.P.L., Reidel.

Bloxham, J., Gubbins, D. & Jackson, A., 1989. Geomagnetic secular variation, *Phil. Trans. R. Soc. Lond., A,* **329**(1606), 415–502.

Bloxham, J., Zatman, S. & Dumberry, M., 2002. The origin of geomagnetic jerks, *Nature,* **420,** 685–687.

Chulliat, A. & Maus, S., 2014. Geomagnetic secular acceleration, jerks, and a localized standing wave at the core surface from 2000 to 2010, *J. geophys. Res.,* **119**(3), 1531–1543.

Eymin, C. & Hulot, G., 2005. On core surface flows inferred from satellite magnetic data, *Phys. Earth planet. Int.,* **152**(3), 200–220.

Finlay, C.C. & Jackson, A., 2003. Equatorially dominated magnetic field change at the surface of Earth's core, *Science,* **300**(5628), 2084–2086.

Gillet, N., Pais, M.A. & Jault, D., 2009. Ensemble inversion of time-dependent core flow models, *Geochem. Geophys. Geosyst.,* **10**(6), Q06004, doi:10.1029/2008GC002290.

Gillet, N., Jault, D. & Finlay, C.C., 2015. Planetary gyre, time-dependent eddies, torsional waves and equatorial jets at the Earth's core surface, *J. geophys. Res.,* **120,** 3991–4013.

Gire, C., Le Mouël, J.L. & Madden, T., 1986. Motions at the core surface derived from SV data, *Geophys. J. R. astr. Soc.,* **84,** 1–29.

Gubbins, D. & Proctor, M.R.E., 1990. Analysis of geomagnetic directional data, *Geophys. J. Int.,* **100,** 69–77.

Holme, R., 2015. Large-scale flow in the core, in *Core Dynamics,* 2nd edn, vol. 8 of *Treatise on Geophysics,* chap. 4, pp. 91–113, ed. Olson, P., Elsevier.

Holme, R. & de Viron, O., 2013. Characterization and implications of intradecadal variations in length of day, *Nature,* **499,** 202–204.

Holme, R. & Olsen, N., 2006. Core surface flow modelling from high-resolution secular variation, *Geophys. J. Int.,* **166**(2), 518–528.

Hulot, G., Khokhlov, A. & Le Mouël, J., 1997. Uniqueness of mainly dipolar magnetic fields recovered from directional data, *Geophys. J. Int.,* **129,** 347–354.

Jault, D., Gire, C. & Le Mouël, J.-L., 1988. Westward drift, core motions and exchanges of angular momentum between core and mantle, *Nature,* **333**(6171), 353–356.

Le Mouël, J.-L., 1984. Outer-core geostrophic flow and secular variation of Earth's geomagnetic field, *Nature,* **311,** 734–735.

Lesur, V., Wardinski, I., Asari, S., Minchev, B. & Mandea, M., 2010. Modelling the Earth's core magnetic field under flow constraints, *Earth Planets Space,* **62,** 503–516.

Lesur, V., Whaler, K. & Wardinski, I., 2015. Are geomagnetic data consistent with stably stratified flow at the core–mantle boundary?, *Geophys. J. Int.,* **201,** 929–946.

Madden, T. & Le Mouël, J.-L., 1982. The recent secular variation and the motions at the core surface, *Phil. Trans. R. Soc. Lond., A,* **306,** 271–280.

Olsen, N. & Mandea, M., 2008. Rapidly changing flows in the Earth's core, *Nat. Geosci.,* **1**(6), 390–394.

Olsen, N., Lühr, H., Sabaka, T.J., Mandea, M., Rother, M., Tøffner-Clausen, L. & Choi, S., 2006. CHAOS—a model of Earth's magnetic field derived from CHAMP, Ørsted, and SAC-C magnetic satellite data, *Geophys. J. Int.,* **166,** 67–75.

Olsen, N., Lühr, H., Finlay, C.C., Sabaka, T.J., Michaelis, I., Rauberg, J. & Tøffner-Clausen, L., 2014. The CHAOS-4 geomagnetic field model, *Geophys. J. Int.,* **197,** 815–827.

Pais, A. & Jault, D., 2008. Quasi-geostrophic flows responsible for the secular variation of the Earth's magnetic field, *Geophys. J. Int.,* **173,** 421–443.

Pais, M.A., Morozova, A.L. & Schaeffer, N., 2015. Variability modes in core flows inverted from geomagnetic field models, *Geophys. J. Int.,* **200**(1), 402–420.

Roberts, P.H. & Scott, S., 1965. On the analysis of the secular variation. 1. A hydromagnetic constraint: theory, *J. Geomagn. Geoelectr.,* **17**(2), 137–151.

Rygaard-Hjalsted, C., Mosegaard, K. & Olsen, N., 2000. Resolution studies of fluid flow models near the core-mantle boundary through Bayesian inversion of geomagnetic data, in *Methods and Applications of Inversion: Lecture Notes on Earth Science,* pp. 255–275, eds Hansen, P.C., Jacobsen, B.H. & Mosegaard, K., Springer.

Sabaka, T.J., Olsen, N. & Purucker, M.E., 2004. Extending comprehensive models of the Earth's magnetic field with Ørsted and CHAMP data, *Geophys. J. Int.,* **159,** 521–547.

Shore, R.M., 2013. An improved description of Earth's external magnetic fields and their source regions using satellite data, *PhD thesis,* The University of Edinburgh.

Silva, L. & Hulot, G., 2012. Investigating the 2003 geomagnetic jerk by simultaneous inversion of the secular variation and acceleration for both the core flow and its acceleration, *Phys. Earth planet. Int.,* **198,** 28–50.

Voorhies, C.V. & Backus, G.E., 1985. Steady flows at the top of the core from geomagnetic-field models: the steady motions theorem, *Geophys. Astrophys. Fluid Dyn.,* **32,** 163–173.

Waddington, R., Gubbins, D. & Barber, N., 1995. Geomagnetic field analysis – V. Determining steady core-surface flows directly from geomagnetic observations, *Geophys. J. Int.,* **122**(1), 326–350.

Wardinski, I., 2004. Core surface flow models from decadal and subdecadal secular variation of the main geomagnetic field, *PhD thesis,* Freie Universitaet Berlin.

Wardinski, I., Holme, R., Asari, S. & Mandea, M., 2008. The 2003 geomagnetic jerk and its relation to the core surface flows, *Earth planet. Sci. Lett.,* **267**(3–4), 468–481.

Whaler, K., 1986. Geomagnetic evidence for fluid upwelling at the core-mantle boundary, *Geophys. J. R. astr. Soc.,* **86**(2), 563–588.

Whaler, K. & Gubbins, D., 1981. Spherical harmonic analysis of the geomagnetic field: an example of a linear inverse problem, *Geophys. J. R. astr. Soc.,* **65**(3), 645–693.

Winch, D., Ivers, D., Turner, J. & Stening, R., 2005. Geomagnetism and Schmidt quasi-normalization, *Geophys. J. Int.,* **160**(2), 487–504.

Zatman, S. & Bloxham, J., 1997. Torsional oscillations and the magnetic field within the Earth's core, *Nature,* **388,** 760–763.

SUPPORTING INFORMATION

Additional Supporting Information may be found in the online version of this paper:

supp1.avi: Time sequence of snapshot flows
supp2.avi: Time sequence of moderately TO-like flows

supp3.avi: Time sequence of difference from the mean of moderately TO-like flows
(http://gji.oxfordjournals.org/lookup/suppl/doi:10.1093/gji/ggw268/-/DC1)

Please note: Oxford University Press is not responsible for the content or functionality of any supporting materials supplied by the authors. Any queries (other than missing material) should be directed to the corresponding author for the paper.

APPENDIX: FLOW AVERAGING FUNCTIONS

We have presented averaging functions for the toroidal and poloidal flow scalars, rather than for components of the flow itself. Since the flow involves derivatives of spherical harmonics, the development for the radial magnetic field component or scalar potentials does not apply directly. We would like to write our estimate $\hat{v}_c$ of a component of the flow, v_c, at a point (θ_0, ϕ_0) on the CMB as

$$\hat{v}_c(\theta_0, \phi_0) = \oint_{\mathrm{CMB}} A(\theta_0, \phi_0, \theta, \phi) v_c(\theta, \phi) \mathrm{d}\Omega, \tag{A1}$$

where A is a function that is well-peaked at (θ_0, ϕ_0) and small elsewhere, enclosing an area of 1 on the unit sphere. Whaler & Gubbins (1981) discuss several definitions of A applicable to models defined on the surface of a sphere.

Before proceeding, we establish an orthogonality relationship for the derivatives of spherical harmonics. Consider the integral

$$\int_0^\pi \frac{\mathrm{d}P_n^m}{\mathrm{d}\theta} \frac{\mathrm{d}P_{n'}^{m'}}{\mathrm{d}\theta} \sin\theta \mathrm{d}\theta. \tag{A2}$$

Integrating by parts, and noting that $\sin\theta$ vanishes at the limits of integration, we have

$$\int_0^\pi \frac{\mathrm{d}P_n^m}{\mathrm{d}\theta} \frac{\mathrm{d}P_{n'}^{m'}}{\mathrm{d}\theta} \sin\theta \mathrm{d}\theta = -\int_0^\pi P_n^m \frac{\mathrm{d}}{\mathrm{d}\theta}\left(\sin\theta \frac{\mathrm{d}P_{n'}^{m'}}{\mathrm{d}\theta}\right) \mathrm{d}\theta. \tag{A3}$$

From Legendre's equation

$$-\frac{\mathrm{d}}{\mathrm{d}\theta}\left(\sin\theta \frac{\mathrm{d}P_n^m}{\mathrm{d}\theta}\right) = \sin\theta \left(n(n+1) - \frac{m^2}{\sin^2\theta}\right) P_n^m \tag{A4}$$

and hence

$$\int_0^\pi \frac{\mathrm{d}P_n^m}{\mathrm{d}\theta} \frac{\mathrm{d}P_{n'}^{m'}}{\mathrm{d}\theta} \sin\theta \mathrm{d}\theta$$

$$= \int_0^\pi P_n^m P_n^{\prime m'} \left(n'(n'+1) - \frac{m'^2}{\sin^2\theta}\right) \sin\theta \mathrm{d}\theta. \tag{A5}$$

Thus,

$$\int_0^{2\pi} \int_0^\pi \left(\frac{m' P_{n'}^{m'} m P_n^m}{\sin^2\theta} \begin{Bmatrix} -\sin m\phi \\ \cos m\phi \end{Bmatrix} \begin{Bmatrix} -\sin m'\phi \\ \cos m'\phi \end{Bmatrix} + \frac{\mathrm{d}P_n^m}{\mathrm{d}\theta} \frac{\mathrm{d}P_{n'}^{m'}}{\mathrm{d}\theta} \begin{Bmatrix} \cos m\phi \\ \sin m\phi \end{Bmatrix} \begin{Bmatrix} \cos m'\phi \\ \sin m'\phi \end{Bmatrix} \right) \sin\theta \mathrm{d}\theta \mathrm{d}\phi$$

$$= \int_0^{2\pi} \int_0^\pi n'(n'+1) P_n^m P_{n'}^{m'} \begin{Bmatrix} \cos m\phi \\ \sin m\phi \end{Bmatrix} \begin{Bmatrix} \cos m'\phi \\ \sin m'\phi \end{Bmatrix} \sin\theta \mathrm{d}\phi. \tag{A6}$$

By orthogonality, the integral vanishes unless $n = n'$, $m = m'$ and the ϕ dependence has both cos or both sin terms, in which case, for Schmidt quasi-normalized spherical harmonics, it equals

$$4\pi \frac{n(n+1)}{2n+1}. \tag{A7}$$

Winch *et al.* (2005) provide an alternative derivation of this result.

This orthogonality relation suggests that we can calculate an averaging function for components of the flow itself by eq. (15), with **c** having elements of the form

$$r_c \left(-\frac{m P_n^m(\cos\theta_0)}{\sin\theta_0} \sin m\phi_0, \frac{m P_n^m(\cos\theta_0)}{\sin\theta_0} \cos m\phi_0, \frac{\mathrm{d}P_n^m(\cos\theta_0)}{\mathrm{d}\theta} \cos m\phi_0, \frac{\mathrm{d}P_n^m(\cos\theta_0)}{\mathrm{d}\theta} \sin m\phi_0 \right) \tag{A8}$$

and **b** of the form

$$\frac{2n+1}{8\pi n(n+1) r_c} \left(\frac{-m P_n^m(\cos\theta)}{\sin\theta} \sin m\phi, \frac{-m P_n^m(\cos\theta)}{\sin\theta} \cos m\phi, \frac{\mathrm{d}P_n^m(\cos\theta)}{\mathrm{d}\theta} \cos m\phi, \frac{\mathrm{d}P_n^m(\cos\theta)}{\mathrm{d}\theta} \sin m\phi \right). \tag{A9}$$

When resolution is perfect, this gives a well-peaked averaging function that has the same value as eq. (14) at the point (θ_0, ϕ_0) at which it is centred; in fact, it is very similar to, but subtlety different from, eq. (14) elsewhere on the CMB. Orthogonality holds so long as **c** and **b** contain pairs of θ and ϕ derivatives of spherical harmonics, so the same formulation provides averaging functions for either the toroidal or the poloidal parts of the flow, or the θ- or ϕ-component of the complete flow, by setting appropriate pairs of elements of **c** and **b** to zero (and the factor 8 in the denominator of **b** to 4 to preserve the amplitude). Hence, this formulation appears at first sight to provide a good candidate flow averaging function. However, it is not well-behaved at the poles—the value depends on longitude, that is, it is not single-valued. It might be possible to overcome the problem by rotating the coordinate system (and the resolution matrix that contains the data distribution information) so that the averaging function is centred on a pole; we have not tried this approach.